*JBMR Plus*, 2025, **9**, ziaf063
https://doi.org/10.1093/jbmrpl/ziaf063
Advance access publication: April 23, 2025
**Research Article**

# Denosumab treatment of giant cell tumors in the spine induces woven bone formation

**Robyn Birch[1,2], Felipe Eltit[3], Dennis Xie[3,4], Qiong Wang[1,5], Nicolas Dea[6], Charles G. Fisher[6], Michael E. Cox[2,3,4], Tony Ng[7], Raphaële Charest-Morin[6], Rizhi Wang[1,2,5,*]**

[1]School of Biomedical Engineering, University of British Columbia, Vancouver, BC V6T 1Z3, Canada
[2]Centre for Aging SMART, Vancouver, BC V5Z 1M9, Canada
[3]Vancouver Prostate Centre, Vancouver, BC V6H 3Z6, Canada
[4]Department of Urological Sciences, University of British Columbia, Vancouver, BC V5Z 1M9, Canada
[5]Department of Materials Engineering, University of British Columbia, Vancouver, BC V6T 1Z4, Canada
[6]Combined Neurosurgical and Orthopedic Spine Program, Department of Orthopedics Surgery, University of British Columbia, Vancouver, BC V5Z 1M9, Canada
[7]Department of Pathology and Laboratory Medicine, University of British Columbia, Vancouver, BC V6T 2B5, Canada

*Corresponding author: Rizhi Wang, Department of Materials Engineering, University of British Columbia, 309-6350 Stores Road, Vancouver, BC V6T 1Z4, Canada (rizhi.wang@ubc.ca).

## Abstract

Giant cell tumors of bone (GCTB) are rare but aggressive, locally destructive tumors. They typically affect young people, significantly reducing their quality of life and increasing mortality rates. Giant cell tumors of bone are composed of osteoclast-like giant cells that respond to increased secretion of RANKL by stromal cells, triggering osteolysis. For over a decade, denosumab, a monoclonal antibody targeting this receptor activator, has been approved as a neo-adjuvant to facilitate surgical resection or in the setting of inoperable tumors. Denosumab treatment has shown rapid pain improvement and tumor size reduction in the spine. Although variable degrees of tumor mineralization have been observed in clinical applications of this drug, the nature of this newly formed mineralized tissue has yet to be determined. To characterize both mineralization and collagen organization in the newly formed bone, we conducted extensive analyses on 4 posttreatment giant cell tumor vertebral samples, involving quantitative backscattered imaging, electron probe microanalysis, and a novel method for determining the alignment of collagen fibrils using second harmonic generation. Additionally, biological mechanisms involved in bone mineralization and matrix formation were analyzed using histological staining and mass spectroscopy. Our results concluded that denosumab treatment after giant cell tumor of bone in the spine was associated with the formation of woven bone and increased mineral density in a matrix of disorganized collagen fibers characterized by increased collagen III content, with the response appearing to depend on patient age and extension of treatment. To our knowledge, this is the first comprehensive material-based study on the bone formed during denosumab treatment for GCTB, providing valuable information on how denosumab affects bone quality and how the reported methodology can be applied to similar studies.

**Keywords:** giant cell tumor, bone mineralization, denosumab, spine, bone microscopy, woven bone

## Lay Summary

Giant cell tumors of bone are rare and aggressive primarily affecting young people causing pain and decreasing quality of life. Denosumab has been used for over a decade to treat these tumors resulting in pain reduction, tumor mineralization, and sometimes tumor shrinkage. In past studies, the nature of bone formation was unclear. In this study, we analyzed denosumab-treated human vertebral samples and discovered that denosumab is associated with a mineralized and disorganized bone matrix. The findings from this study highlight the possible influence of patient age and treatment duration, helping us gain insight into bone quality formed during denosumab treatment.

**Received:** November 22, 2024. **Revised:** March 22, 2025. **Accepted:** April 2, 2025

## Graphical Abstract

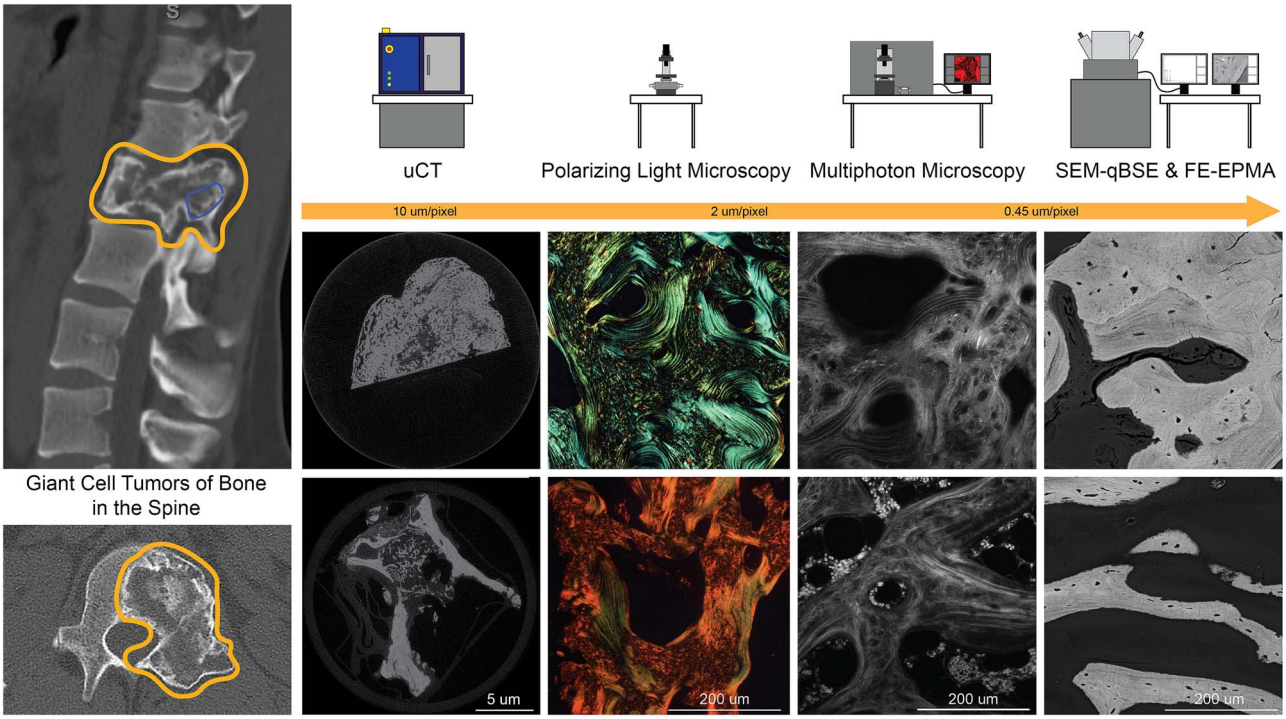


## Introduction

Giant cell tumors of bone (GCTB) are aggressive, benign tumors that predominantly affect individuals before their fourth decade of life.[1–3] Giant cell tumors of bone have low incidence rates (1-1.6 cases per million inhabitants per year),[3,4] representing less than 8% of all bone tumors,[5,6] localizing in areas of trabecular bone, such as the epiphysis of long bones, the sacrum, and vertebrae. Spinal GCTBs represent less than 10% of all GCTB cases,[7,8] but their proximity to vital organs reduces surgical options—unlike GCTBs appearing in the appendicular skeleton that can simply be resected—dramatically affecting prognosis and survival. Giant cell tumors of bone are characterized by multinucleated, osteoclast-like giant cells that express RANKL.[9,10] These cells are present in high quantities and are surrounded by neoplastic mononuclear spindle-like stromal cells.[2,11,12] Although the precise etiology of GCTBs is not fully understood, it has been more recently characterized by a genetic mutation of the H3 histone family member 3A gene (H3F3A) in stromal cells.[13] Another key element in the pathogenesis is the abnormal secretion of RANKL by the stromal cells.[14,15] RANKL is a cytokine that serves a key role in the bone remodeling process.[16,17] Its best-understood function is to induce the differentiation of osteoclast precursors into mature osteoclasts through binding to its receptor, RANK, initiating osteoclastogenesis. Overexpression of RANKL has been hypothesized to be the cause of the many osteoclast-like giant cells found in GCTBs by stimulating monocyte migration to the tumor tissue, and fusion to form the osteoclast-like multinucleated giant cells,[14,18] contributing to their osteolytic nature, leading to considerable bone resorption at the tumor site.[12,14,15]

Clinically, spinal GCTBs are locally destructive lesions presenting with pain, possible neurologic compromise, affecting mobility,[9] and increased fracture risk.[11] While considered to be benign, GCTBs have a high recurrence rate and occasionally do form lung metastases, which represents a challenge in therapeutical management. Currently, en bloc resection with marginal-wide margins (a more aggressive resection) is the preferred treatment of spinal GCTB.[2,11,19] Due to the proximity of vital functional structures in the spine, as well as the need for clear margins to prevent primary local recurrence, the tumor is ossified using subcutaneous injections of denosumab. Denosumab is the only drug approved for treating unresectable GCTB or cases where severe morbidity will occur as a result of surgical resection.[9,20,21] Denosumab is a monoclonal antibody that interferes with the bone remodeling process, binding with RANKL, and suppressing osteoclast formation and survival.[10,11] Denosumab treatment has been associated with the promotion of bone remodeling[6] and pain reduction[1] resulting from reduced bone destruction as a result of osteoclast inhibition.[22] Several studies demonstrated denosumab-mediated elimination of giant cells[1,6,9,20]; however, since the neoplastic cells in GCTB are the stromal cells, significant local recurrence or tumor progression has been reported after discontinuing denosumab.[11,19,23,24] While there are many benefits of using denosumab in GCTB treatment, its use is also associated with rebound phenomena[11,25] and malignant transformation of the benign tumors following treatment.[26]

Woven bone formation in denosumab-treated GCTBs has been previously described based solely on histological observations.[10,27,28] However, no detailed analysis of the woven bone quality and structure was completed, leaving a gap in our understanding of how denosumab treatment impacts bone homeostasis and structure in cases of GCTB. Such knowledge is extremely valuable in helping physicians develop

appropriate therapeutic plans and surgical procedures. Due to the rarity of spinal GCTB, the study of bone quality has been challenging, with clinical imaging tools lacking the ability to capture microscopic details of bone structure. Over the last several years, we had 4 patients who underwent resection for a GCTB after being treated with neoadjuvant denosumab at Vancouver General Hospital. This gave us opportunities to conduct in-depth analyses of the mineralized vertebral tissues retrieved during surgery. Our objective is to apply high-resolution imaging and comprehensive material analyses to examine the microscopic effects of denosumab on the bone formation and mineralization processes of spinal GCTBs.

## Materials and methods

### Patients

Four patients (7 cores), 1 male and 3 females (mean age = 37.5), who underwent resection for spinal GCTB after being treated with neoadjuvant denosumab were recruited in this study (samples further outlined in Table S2). The analyses conducted under this study have been performed under approval of the ethics board of the University of British Columbia (H22-03461). All patients consented to tumor sample collection through local biobanking protocol (H19-01413). Giant cell tumors of bone patients who received neoadjuvant denosumab treatment were administered 120 mg denosumab via subcutaneous injection monthly, with additional doses administered on days 8 and 15 in the first month of treatment. They were subjected to denosumab treatment for periods of 3, 5.5, 6, and 7 mo (samples 1 to 4, respectively) before tumor resection. A total of 7 healthy cadaveric vertebrae controls (12 cores), 6 male and 1 female (mean age = 77) were acquired from UBC's Body Donation Program (H21-02668, samples further outlined in Table S3). While the healthy vertebral tissue could not be age or sex-matched, the vertebral location was matched.

### Sample preparation

All surgically resected GCTB samples were stored at −20 °C until processing. Pathological GCTB tissue was fixed in 10% formalin for 48 hr and stored in 1× PBS at room temperature (21 °C) until dehydration was completed. The vertebral control cores were fixed in 70% ethanol for 2 wk and stored in 70% ethanol under constant refrigeration (4 °C). Further details regarding sample acquisition are outlined in the Supplementary material and in Figure S1, S2.

### Micro-computed tomography

The bone microarchitecture was analyzed using micro-computed tomography ($\mu$CT). Samples were placed into a sample holder (30 mm × 75 mm) and scanned using high-resolution $\mu$CT ($\mu$CT 35, SCANCO Medical AG) using the following parameters: isometric voxel size = 10.0 $\mu$m, source voltage = 70 kVp, intensity = 114 $\mu$A, 8 W, integration time = 500 ms. To avoid the inclusion of damaged tissue or surgical debris, a reduction factor was applied to the selected volume before microarchitecture analysis (details in Supplementary material and Figure S3). Microarchitectural parameters (BV/TV, Tb.N, Tb.Sp, Tb.Th, Conn.Den, mean Ca) were extracted using a built-in SCANCO segmentation algorithm (SCANCO Medical AG).

### Mineral composition measurement

Samples underwent dehydration through a graded acetone series (70%, 80%, 90%, for 48 hr, then 2 series of 100% for 72 hr each). Spurr resin was prepared following the manufacturer's instructions (Ted Pella Inc.). Samples were infiltrated in acetone/Spurr under vacuum conditions (50% for 72 hr, 80% for 72 hr, 100% Spurr for 72 hr twice at 4 °C) before curing in 100% Spurr at 55 °C overnight. The cured samples were ground with a series of carbide grinding papers (240, 320, 400, 600, 800, 1000, 1200; Allied High Tech Products Inc. and Buehler Ltd.) to expose ROIs in the samples and polished to a mirror surface finish with sequential 6 and 1 $\mu$m water-based monocrystalline diamond suspension (Allied High Tech Products Inc.).

Quantitative backscattered electron imaging (qBSE, a.k.a. qBEI) was performed using an SEM (FEI Quanta 650 SEM) in backscattered electron mode. The imaging was completed on carbon-coated, polished resin blocks, using the following parameters: voltage = 20 kV, working distance = 15 mm, spot size = 6, and magnification = 200×. Between 6 and 16 ROIs per sample were imaged, acting as a true representation of the entire sample. Each image captured during measurement had dimensions 636 $\mu$m × 457 $\mu$m and a resolution of 1535 pixels × 1103 pixels. During imaging, the BSE signal was calibrated using a standard carbon with a gray level of 30±2 and aluminum with a gray level of 225±2. Field-emission electron microprobe analysis (FE-EPMA) complemented this analysis measuring the Ca/P ratio, with acquisition details outlined in the Supplementary material.

### Lacunae morphological analysis

Using images from qBSE, the same ROIs were used to evaluate the properties of the lacunae: lacunae density, dimensions, axis ratio, and shape. Areas of lamellar bone were manually masked separately from the woven bone in ImageJ.[29] Using techniques previously described,[30] regional property analyses were achieved in MATLAB (R2022b) on lacunae segmented using thresholding. Nonlacunar void spaces were manually excluded, and lacunar morphology parameters were calculated for each image based on the 2 bone morphologies visualized: disorganized and lamellar.

### Second harmonic generation

Imaging was performed on an Olympus Multiphoton Laser Scanning Microscope FV1000 (MPM, Olympus Co.) to image embedded, polished samples. A 25×, NA = 1.05 water immersion objective lens was used (XLPN 25× water immersion, Olympus Co.), and samples were imaged at an excitation wavelength of 800 nm. Images were acquired in Fluoview FV1000 with image dimensions of 509 $\mu$m × 509 $\mu$m, a resolution of 1024 pixels × 1024 pixels, at a sampling speed of 10.0 $\mu$s/pixel using Kalman Integration during z-stack acquisition.

ROIs were evaluated for each bone type, 76 × 76 pixels in size (pixel resolution = 0.497 $\mu$m/pixel), with a depth of 15 $\mu$m (3 $\mu$m step size × 5 slices) to evaluate changes in alignment through trabeculae. Similar to past studies,[31,32] a custom MATLAB program was designed to process ROIs using an FFT and radial summations to determine the alignment of fibers. A "min-max" ratio eqn (1) was used to quantitatively evaluate the fiber alignment for each ROI based on the

magnitude of the FFT frequency summation:

$$\text{Alignment Ratio} = 1 - \frac{\text{minimum intensity sum}}{\text{maximum intensity sum}} \quad (1)$$

Values of alignment closer to 1 indicate strong alignment of the collagen fibers, while values closer to 0 indicate disorganization or poor alignment.

### Proteomic analysis

Proteins were extracted from formalin-fixed paraffin-embedded demineralized bone sections ($6 \times 5$ $\mu$m sections). Sections were deparaffinized and further processed before peptide collection and analysis using methods outlined in the Supplementary material.

### Histological staining techniques

Bone tissue was demineralized in 10% formic acid for 4-6 d based on sample size. The samples were dehydrated in a graded ethanol series (70%, 80%, 90%, 95%, 100% $\times$ 3) for 1.5 hr each, cleared in xylene substitute (Histoclear II, Electron Microscopy Sciences) twice for 3 hr each, and paraffin-embedded. Serial, 5 $\mu$m thick, sections were prepared on a microtome (Leica RM2235, Leica Biosystems), mounted on microscope slides, and subjected to basic histochemical staining with toluidine blue, picrosirius red, Goldner's trichrome, and H&E. Immunohistochemistry was completed using standard protocols[30] (outline and primary antibodies in the Supplementary material, Table S1) and incubated in diaminobenzidine reagent (DAB Substrate Kit) for visualization of the immunodetection. All slides were mounted using a mounting medium (Epredia, Fischer Scientific). Microscopic observations were made using an upright brightfield microscope (Carl Zeiss) and imaged using a cooled camera and ZEN software (Zeiss). Further image processing was completed in Adobe Photoshop (v25.12.0).

### Statistical analysis

Analysis was performed in MATLAB (R2022b) using built-in statistical functionality. Data was first assessed using a Shapiro–Wilks test for normality. Based on consistent non-normality in the data, further analysis was achieved with the Mann–Whitney *U*-test for unpaired datasets with 2 groups or a Kruskal–Wallis test for analysis across several unpaired samples. All statistical analyses are reported as $^{*}p < .05$, $^{**}p < .01$, and $^{***}p < .001$.

## Results

### Denosumab-treated GCTBs show abnormal bone formation occasionally accompanied by newly formed trabeculae

We evaluated the qualitative characteristics of 7 denosumab-treated GCTB samples from 4 patients (Table S2) and 9 nonpathological (healthy) cadaveric vertebrae cores from 5 patients (Table S3). All quantitative and qualitative $\mu$CT data is available in Table S4 and Figure S4. A high variability in morphology of mineralized bone of GCTBs after denosumab treatment was observed compared to healthy control vertebrae (Figure 1; Figure S4). While healthy control vertebrae show the characteristic rod-plate trabecular structures (Figure 1A), denosumab-treated GCTBs are characterized by the presence of irregularly shaped calcified tissue (Figure 1B-E), frequently showing a fine granular component occupying the whole marrow spaces (Figure 1B-D). This irregular, disorganized bone was present in the 4 analyzed GCTB samples, broadly distributed, and in some cases surrounded by the remaining vertebral cortical shell (Figure 1B, Sample 1). The amount of disorganized bone also varies from diffuse and scattered calcified tissue in a mostly noncalcified matrix (Figure 1C and D, Samples 2 and 3) to a solid mass completely calcified with minimal noncalcified spaces (Figure 1E, Sample 4). These characteristics are associated with variations in both BV/TV and Tb.N across samples.

To observe further details, quantitative qBSE SEM imaging was performed on 4 GCTB samples and 5 vertebral controls, measuring between 6 and 16 areas of disorganized and lamellar bone (if present). We observed the bone in denosumab-treated GCTBs to have irregularly shaped trabeculae (Figure 1B), irregular borders showing diffuse edges (open arrows in Figure 1B, D, and E), and porous patterns on the trabecular surface (closed arrows in Figure 1C). Another noteworthy feature is an apparent increased porosity of the disorganized bone, with increased quantity and irregularly shaped lacunae (open arrowheads in Figure 1B-E). While most of the bone in the denosumab-treated GCTBs showed an irregular composition, in 3 cases, new lamellar bone deposition was observed on the disorganized bone surfaces (open and closed squares, respectively in Figure 1B, D, and E).

Combined, these results show that the inhibition of the RANKL pathway by denosumab treatment triggers the formation of reparative bone, primarily composed of an irregular calcified bone matrix, that in some cases may transition to the formation of lamellar structures.

### Denosumab-treated GCTBs show an increase in bone volume

We continued our analysis with microarchitectural quantification of the trabecular structure in denosumab-treated GCTBs. Out of the 7 analyzed samples, 5 showed a higher bone volume/total volume (BV/TV) than the healthy bone, and 2 showed a BV/TV slightly lower than the healthy bone (Figure 2A). The increased BV/TV is accompanied by increased trabecular number (Tb.N, Figure 2B; Figure S5A), which reduces trabecular separation (Tb.Sp, Figure 2C), and increases trabecular connectivity (Conn.Den, Figure 2D). Based on the limited number of cases available and high variance in the $\mu$CT results, the only clinical variables that showed potential association with the increased BV/TV are patients' age (Figure S5B) and duration of denosumab treatment (Figure S5C). These results show that the inhibition of the RANKL pathways through use of denosumab elicit mineralization of the GCTB-affected extracellular matrix.

### Denosumab-treated GCTBs show variance in mineral properties and composition between bone types

Minimal trends in the $\mu$CT results led us to local qBSE imaging and FE-EPMA to analyze the mineral content and composition of the disorganized bone in denosumab-treated GCTBs. Initial observation highlighted a significantly higher mineral content in disorganized bone than that observed in the healthy lamellar controls (20.83±1.41 vs 21.43±1.67 Ca wt%). The

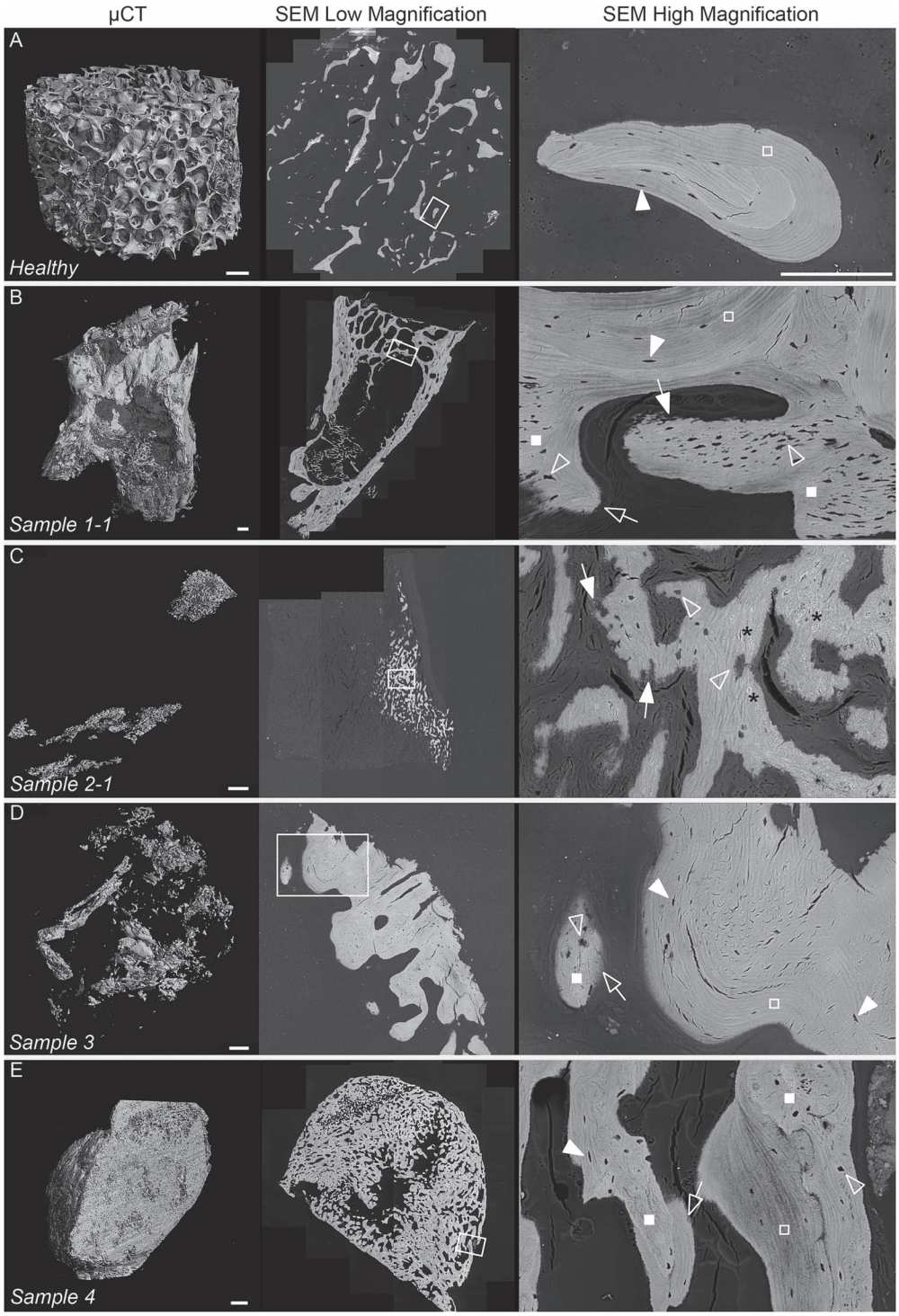


**Figure 1.** Micro-computed tomography 3D renderings of full-size cadaveric and surgically resected vertebrae (left column), followed by a stitched SEM low magnification image of the specimen (middle column), and a high magnification image of a selected ROI, outlined in white on the low magnification image (right column). (A) A vertebral matched healthy control demonstrating normal trabecular lamellar structure (open box) and ovoid lacunae (closed arrowhead) oriented along the lamellar major axis. (B) Sample 1, a mixed bone type with lytic-like disorganized bone formation inside large voids within original cortical and trabecular bone, with lamellar bone (open box) on the surfaces of woven bone (closed box) and irregular diffuse edges and porous erosive-like patterns (arrows, open and closed). The presence of ovoid lacunae (closed arrowheads) in lamellar bone is accompanied by round or irregular-shaped lacunae (open arrowheads) present in increased density in the woven bone. (C) Sample 2, a disorganized bone sample with lytic-like woven bone formation (closed box), porous indentations on the trabecular surfaces (closed arrows), and increased mineral deposits indicated by asterisks. (D) Sample 3, a lytic-like disorganized bone sample, with evidence of normal lamellar structure (open box), accompanied by adjacent woven bone (closed box), with ovoid (closed arrowhead), and nonovoid (open arrowhead) lacunae presence in adjacent bone types. (E) Sample 4, an osteoblastic sample characterized by thick trabeculae demonstrating an irregular, woven calcified matrix (closed box), with instances of lamellar bone forming on the surface (open box). Again, ovoid lacunae (closed arrowheads) are found in lamellar bone with round or irregular-shaped lacunae (open arrowheads) present in increased density in the woven bone. The scale of $\mu$CT renders = 1 mm, and all SEM high magnification images = 200 $\mu$m.

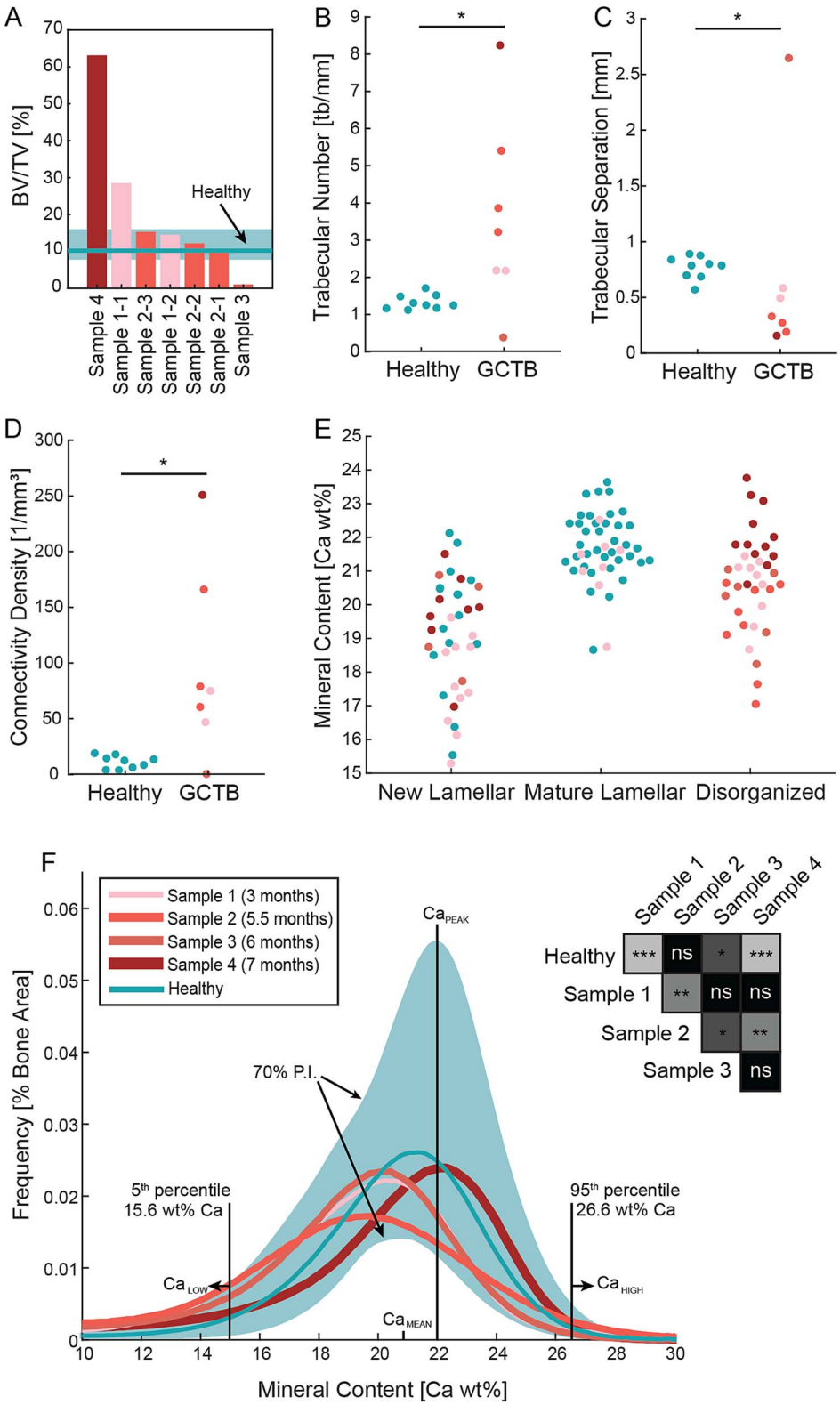


**Figure 2.** Analysis of bone morphological parameters acquired using $\mu$CT and mineral density of each sample measured using SEM-qBSE. (A) A waterfall plot of the bone volume/total volume (BV/TV) grouped by individual scans. The horizontal line indicates average healthy BV/TV, with the transparent box representing the minimum to maximum range. (B–D) Scatterplots of trabecular morphology quantification of the healthy and GCTB groups based on $\mu$CT evaluation. Statistical significance for each parameter was evaluated using a Mann-Whitney test. (E) Scatterplot of mineral content grouped by bone type. (F) A bone mineral density distribution using average histogram data for all controls and each GCTB sample. Statistical significance was evaluated between samples using a Kruskal–Wallis test. *$p < .05$, **$p < .01$, and ***$p < .001$, ns = not significant.

**Table 1.** Summary of Ca/P ratio for different bone types.

| Bone type | Ca/P ratio (median) | Standard deviation | Difference from healthy |
|---|---|---|---|
| **Healthy** | 1.643 | 0.076 | Not applicable |
| **Lamellar** | 1.572 | 0.086 | ** |
| **Disorganized** | 1.524 | 0.110 | *** |

**$p = 0.0031$, ***$p = 6.5 \times 10^{-8}$.

previously described trabecular bone formed in denosumab-treated GCTBs (Figure 1B, D, and E) has significantly lower mineral content (18.75±1.64 Ca wt%, Figure 2E) than both disorganized bone and healthy trabecular bone. Further investigation demonstrated the possible influence of treatment duration (Figure 2F; Figure S6A) and age (Figure S6B) on GCTB mineral content when grouped by sample. The values for the Ca/P ratio of disorganized bone (1.52±0.11) were lower than healthy controls (1.64±0.076), and lower than the new lamellar bone (1.57±0.086) (Table 1; Figure S7). Together, these results demonstrate increased mineralization with impure hydroxyapatite formation in the disorganized calcified matrix, influenced by an extension of denosumab treatment time.

## Increased lacunae number, with increased roundness and area characterize disorganized bone in denosumab-treated GCTBs

Our qBSE observations suggested differences in the number and shape of the void spaces, presumed to be lacunae, in the disorganized bone. Based on laser scanning confocal microscopy completed on rhodamine-stained embedded bone sections (Supplementary material), we confirmed the presence of a lacuna-canalicular network in the calcified bone matrix, with increased density in the disorganized bone (Figure S8).

Using qBSE images, we assessed lacunae density, area, and shape. The denosumab-treated disorganized bone demonstrated a 125% increase in lacunar density compared to healthy control bone (median, IQR: 470.10, 347.91 vs 208.84, 92.81 lacunae/mm$^2$, respectively). This increased lacunar density is also observed in the GCTB lamellar bone (410.32, 249.07 lacunae/mm$^2$, Figure 3A). The GCTB bone we described shows increased lacunae number in both disorganized (48, 43) and lamellar matrix (40, 81) from the healthy normal (19, 15, Figure 3B). The lacunae area presented differences between bone types, with the disorganized bone type showing bigger lacunae (26.79, 9.21 $\mu$m$^2$) than the healthy (24.21, 6.77 $\mu$m$^2$) and GCTB lamellar bone (19.70, 6.55 $\mu$m$^2$, Figure 3C). This increase in area was shown to be a result of a longer minor axis (Figure 3D) in disorganized bone (3.66, 0.65 $\mu$m) from normal (3.24, 0.78 $\mu$m healthy controls, 2.94, 0.53 $\mu$m GCTB lamellar bone), as opposed to differences in major axis length which showed minimal differences from the healthy. This increase in minor axis length causes the length axis ratio of lacunae in disorganized bone (2.25, 0.35) to decrease compared to healthy controls (2.95, 0.59), a further decrease from GCTB lamellar bone (2.72, 0.67) (Figure 3E). This decrease in the length axis ratio implies an increase in circularity, which we observed in disorganized bone lacunae (0.898, 0.085) when compared to those of newly formed GCTB lamellar and healthy lamellar bone (0.855, 0.112 vs 0.789, 0.072) (Figure 3F).

These results suggest the bone formation process during denosumab treatment has caused abnormal entrapment of osteocytes, creating abnormally shaped lacunae within the irregular calcified bone matrix, possibly due to rapid deposition of extracellular matrix resulting in increased quantity of lacunae. The increased circularity of lacunae, combined with a lack of lamellar structure suggests irregular collagen deposition before subsequent calcification in the disorganized bone matrix.

## Disorganized denosumab-treated GCTB bone is characterized by a lack of collagen alignment

From previous qBSE imaging, a lack of visible striations in the disorganized bone indicated differences in the collagen matrix. We used second harmonic generation (SHG) to visualize collagen organization in our denosumab-treated GCTB samples. In total, we analyzed 4 GCTB samples and 5 vertebral controls, identifying 2-3 ROIs per bone type present in each image (Figure S9). For each ROI, an alignment across a depth of 15 $\mu$m (5 images × 3 $\mu$m) was analyzed to establish differences between disorganized and lamellar trabecular tissue formed during denosumab treatment. The alignment of healthy vertebral fibers and lamellar fibers in denosumab-treated tissue produces a significantly higher alignment ratio (0.778±0.068 and 0.709±0.064, respectively), resulting from the sheet-like orientation of collagen in the formation of lamellar bone. The disorganized bone produced a significantly lower alignment ratio (0.573±0.081, Figure 4A, validated in Figure S10). Furthermore, the alignment ratio in disorganized tissue demonstrated increased standard deviation (Table 2; Table S5), indicating an increased change of alignment in the collagen fibers with depth in each slice. Lamellar bone in our healthy group as well as the lamellar GCTB group demonstrated smaller deviations, a result of fiber alignment maintaining consistency with depth. Not only can the alignment ratio indicate the degree of alignment, but we can qualitatively analyze the regions with varying degrees of organization (Figure 4B). Disorganized bone shows random intensities of fibers, with varied thickness and orientation (Figure 4C), whereas distinct linear patterns with intense white and black repeated striations are visible in lamellar bone (Figure 4D). These qualitative differences are visualized using a radial summation of the FFT for each ROI demonstrating an intense peak when aligned and a broader, flattened curve when disorganized.

Based on the combined quantitative and qualitative information, we conclude that the collagen has formed with abnormal organization in the mineralized GCTB tissue, resulting in shorter appearing, randomly oriented fibers, whereas lamellar bone demonstrates high alignment following the sheet-like patterns expected in healthy lamellar bone. The presence of both patterns in GCTB denosumab-treated tissue supports our earlier hypothesis that an irregular reparative calcified bone matrix is present, with the transition to lamellar bone formation occurring on the irregular bone surfaces.

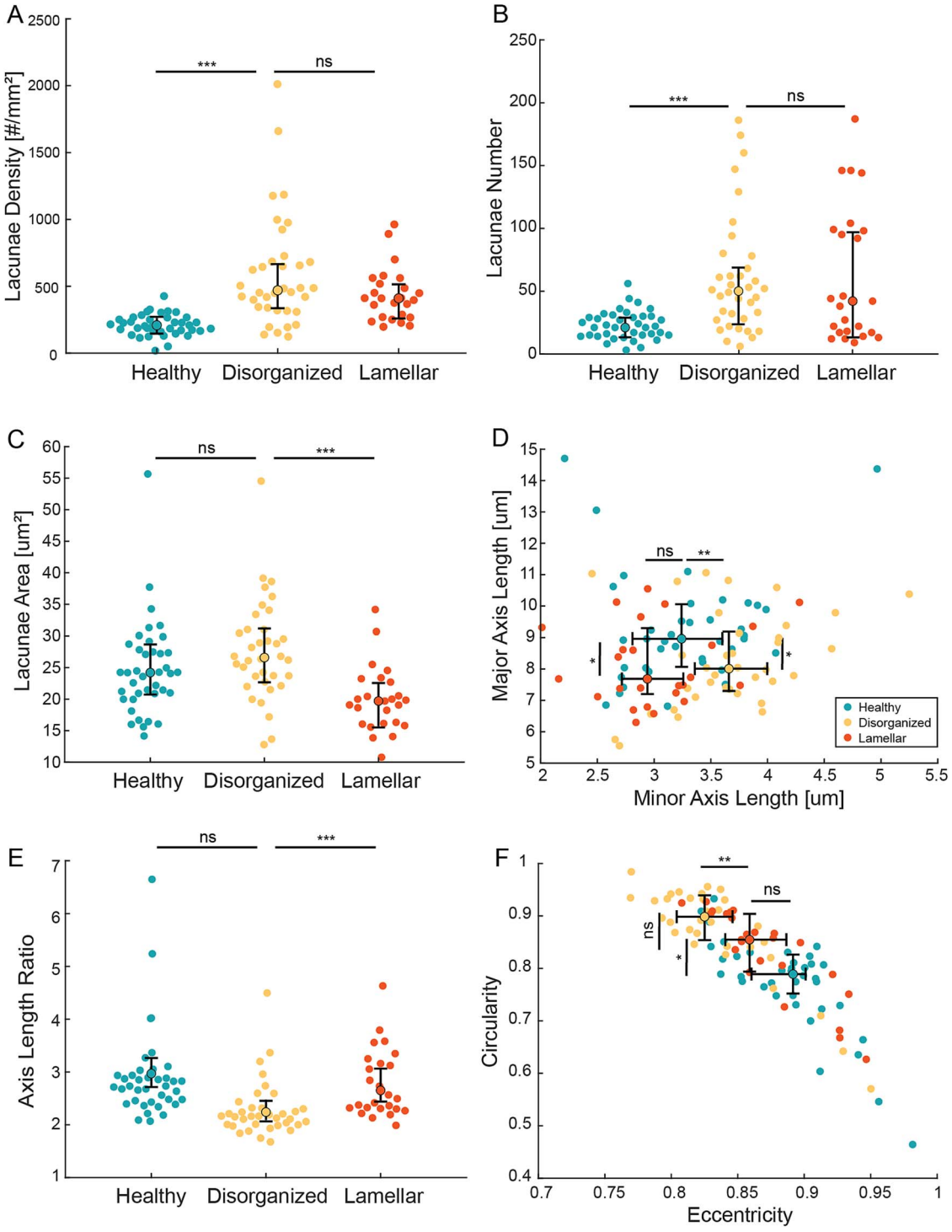


**Figure 3.** Lacunar morphology characterization scatterplots with median ± IQR for healthy vertebrae and both disorganized and lamellar bone from GCTB samples. (A) Lacunae density, (B) lacunae number, (C) individual lacunae area, (D) distribution of major and minor axis length, (E) major axis to minor axis length ratio, and (F) measure of lacunae roundness. $^{*}p < .05$, $^{**}p < .01$, and $^{***}p < .001$, ns = not significant. Number of analyzed lacunae in healthy lamellar areas = 809, lacunae in GCTB lamellar areas = 1457, and in GCTB disorganized areas = 2108.

## Altered protein content in denosumab-treated GCTBs indicates a state of repair in the calcifying bone matrix

While the main component in connective tissues is collagen fibers, they depend on many proteins and proteoglycans to generate a mature structure. Our previous observations of abnormal collagen organization and calcification suggest alterations in the protein content of the mineralized denosumab-treated GCTB. We performed tandem mass tag (TMT) spectrometry of 4 GCTB samples from our 4 patients and compared them with 3 healthy vertebrae samples from 2 donors. We observed clustering of healthy vertebrate in a single family, showing clear differences with the denosumab-treated group, which in turn cluster as a single family (Figure 5; Figure S11A).

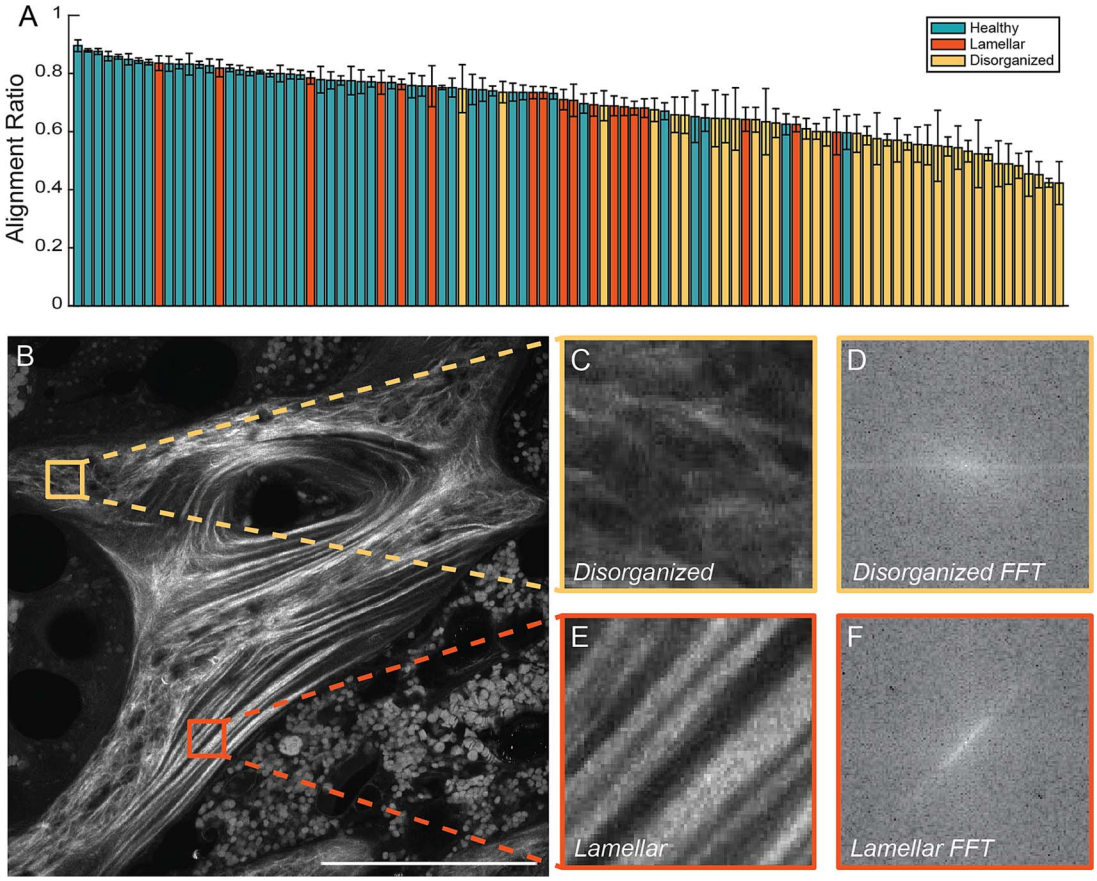


**Figure 4.** SHG collagen fiber alignment measurement. (A) A waterfall plot to illustrate the alignment present in the SHG images with grouping of bone types based on alignment ratio. The healthy treatment group, and the normal GCTB lamellar bone fall to the left side of the plot, indicating the fibers are more aligned—a result of pixels of the same intensity, directed in the same direction. The GCTB disorganized bone falls to the far right of the waterfall plot due to the decreased alignment of the fibers, a result of disorganized collagen fibers, seen by randomized intensities in different directions. (B) An ROI of sample 1 containing both disorganized and lamellar bone tissue, depicting a lamellar ROI, and a disorganized ROI. Branching trabeculae are visible in greyscale, with the collagen in the normal lamellae appearing brighter with linear striations. The collagen in the disorganized regions appears thinner, with variable intensity and random alignment. (C) A selected disorganized ROI, and (D) its resultant FFT illustrating minimal alignment of the fibers. (E) A selected lamellar ROI, and (F) its resultant FFT illustrating a preferred direction of alignment of the fibers. The resulting FFTs were rotated 90° for orientational analysis. Scale bar = 200 $\mu$m.

**Table 2.** Summary of collagen fiber alignment.

| Bone type | Alignment ratio (median) | Standard deviation | Difference from healthy |
|---|---|---|---|
| **Healthy** | 0.778 | 0.068 | Not applicable |
| **Lamellar** | 0.709 | 0.064 | Not significant |
| **Disorganized** | 0.573 | 0.081 | *** |

***$p = 2.9 \times 10^{-14}$.

When identifying proteins that are differentially expressed in the analyzed samples (list in Table S6), we found that upregulated extracellular matrix proteins in denosumab-treated GCTBs were collagen type III (Figure S10B), which is characteristic of wound healing tissues, the network-forming collagen types IV and X, and the member of the FACIT family (fibril-associated collagens with interrupted helices) collagen type XIX. These are accompanied by the muscle-related proteins TPM2, MYH7B, the spermatogenesis-related proteins SPATA31E1, ACTRT1, a calcium-dependent protein C2CD4D (whose functions have not been described but are upregulated in some cancers), and a zinc finger DHHC-Type Palmitoyltransferase (ZDHHC23). Consistently, when we analyze the protein content associated with functional groups, we found mostly down-regulated functional groups in the denosumab-treated GCTBs that are related to immune system functions (Figure S11C). In conclusion, the presence of elevated levels of collagen III, accompanied by nonfibrillar collagens suggests the presence of reparation-related extracellular matrix in denosumab-treated GCTBs.

## Denosumab-treated GCTB tissue exhibits 2 distinct bone types and bone mineralization activity

Our protein analysis suggested that differences in protein content may influence the morphological and structural differences observed between the denosumab-treated irregular GCTB tissue and healthy trabecular bone. To determine

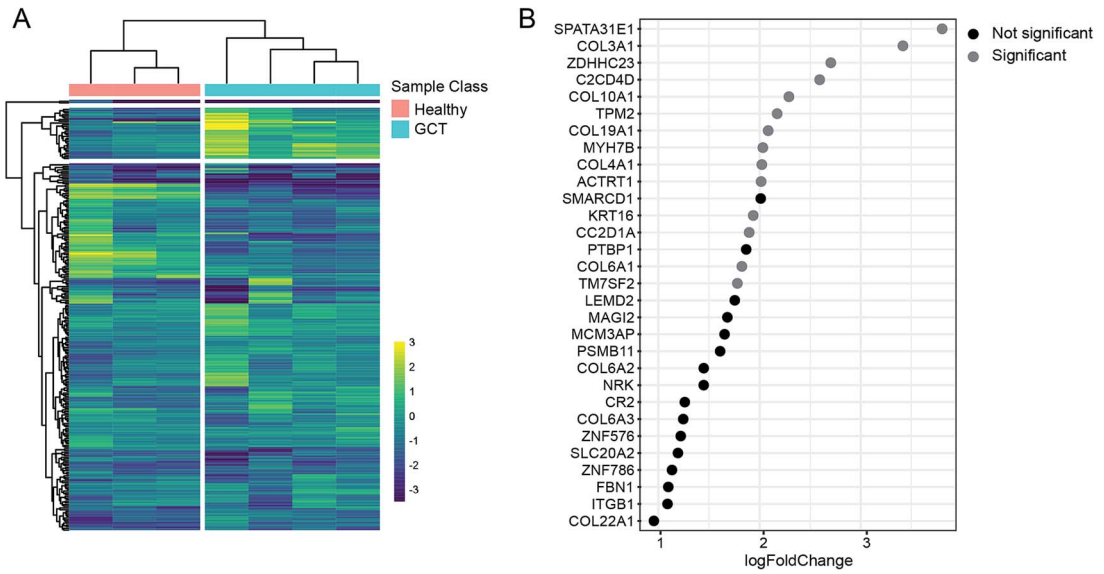


**Figure 5.** Visualization of protein clustering. (A) Dendrogram showing clustering of the sample groups with similar protein expression and clustering based on similar expression patterns. (B) A ranked order of the protein cluster plotted by the protein fold change.

whether these differences are associated with specific locations of extracellular matrix proteins within the tissues, histological, histochemical, and immunohistological characterization was performed. H&E staining showed different histological patterns with visible striation patterns present in the trabeculae, a pattern lacking in the disorganized bone of denosumab-treated GCTBs (Figure 6A). Using toluidine blue, a cationic dye, the disorganized bone was stained with greater intensity than the adjacent lamellar bone (Figure 6B) and healthy vertebral trabecular bone (Figure S12B and N) implying more negatively charged molecules in the irregular bone. Sirius red provides a visualization of the disorganized fibers when viewed under optical polarizing light (Figure S12E and Q). The parallel lamellar fibers produce a signal that is more similar in color in long striated patterns, indicating an aligned collagen fiber. The disorganized tissue appears as short, thin fibers that are arranged in varied directions with varied birefringence and color (Figure S12Q), aligning with our previous observations surrounding an irregular and disorganized collagen framework seen in SHG.

In all GCTB samples, we observed collagen III staining in the disorganized bone (arrows in Figure 6C), which was absent in the newly formed trabeculae when they were present (arrowheads in Figure 6C). Other extracellular matrix proteins such as osteopontin, osteomodulin, and proteoglycan decorin were also found in the extracellular matrix of the disorganized bone in denosumab-treated GCTBs (close arrowheads in Figure 6D-F), with negative or lower expression in the adjacent trabeculae (open arrowheads Figure 6D-F) and healthy trabecular vertebral bone (Figure S12I-K, U-W). The presence of decorin and osteomodulin in the mineralization process as nucleators initiating the crystal deposition,[33,34] accompanied by the regulator osteopontin[35–37] suggests that there is an active process of biomineralization in the organic matrix. In addition, their colocalization with collagen III suggests the mineralized tissue corresponds to a form of early reparative bone formation driven by denosumab treatment in GCTB lesions.

## Discussion

Giant cell tumors of bone are a rare benign tumor and are typically observed in adolescents and young adults, dramatically impacting the quality of life. The use of denosumab as a stand-alone treatment or neoadjuvant for GCTBs has shown promising results for patients with an unclear understanding of its effects on trabecular bone and mineralization of tissue. The presence of a woven bone morphology has previously been suggested in denosumab-treated GCTBs, but there is no follow-up related to its structure and possible mechanisms of bone remodeling.[10,25,26] To the best of our knowledge, our study is the first comprehensive, in-depth evaluation of the structural and biological characteristics of mineralized GCTB tissue after denosumab treatment. In this study, we described a calcified tissue with high mineral density, irregular collagen fiber organization, increased size and quantity of cell lacunae, all qualities characteristic of woven bone. In some cases, we observed lamellar bone deposited on the surface of woven bone, resembling the event of bone repair and remodeling, accompanied by high collagen III content. Combined, these results demonstrated that the blocking of this RANKL pathway is essential in the treatment of GCTBs by promoting bone tissue repair and calcification.

Initial denosumab approval in 2010 was for the prevention of fractures, focusing on reducing bone loss in cases of metastasis (Xgeva, Amgen) and osteoporosis (Prolia, Amgen). In oncological settings, the dosage and frequency are more aggressive, as opposed to a lower-dose regimen used in cases of osteoporosis. Denosumab treatment increases patients' bone mineral density while reducing bone turnover markers.[38–40] FREEDOM, a phase III clinical trial that enrolled 7868 postmenopausal women, found an increase in BMD of the lumbar spine, measured with DXA.[41] Later approval was granted for cases of unresectable or severe spinal GCTB, with inhibition of giant cells resulting in a decrease in pain, ossification of the tumor, and possible tumor shrinkage. A phase II clinical trial on the treatment of 37 GCTB patients was reported in 2010,[9] demonstrating safety and a low rate of adverse effects in therapeutic dose of denosumab. Two years later,

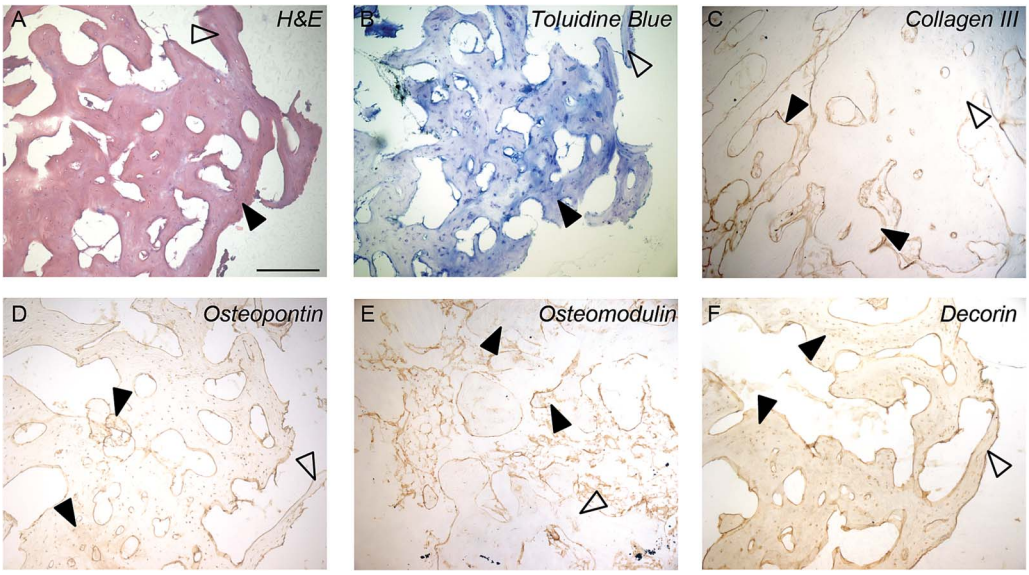


**Figure 6.** Histological and immunohistochemical analysis showed differences in staining between the lamellar and disorganized bone in the GCTB samples. (A) H&E, (B) toluidine blue staining results in a staining pattern across the entire matrix, with differences in the stain intensity result in disorganized bone staining darker (closed arrowheads) than the lamellar regions (open arrowheads). The abnormal lacunae tend to stain darker along the lacunar edges, whereas lamellar bone lacunae tend to stain with a clean, smooth surface. (C) Collagen III, (D) osteopontin, (E) osteomodulin, and (F) decorin immunohistochemical staining, demonstrating increased staining in the disorganized matrix (closed arrowheads) compared to the lamellar matrix (open arrowheads). Images correspond to GCTB sample 4. Scale bar = 200 $\mu$m.

the same group reported a reduction in tumor size, with a decrease in RANKL-positive stromal cells after denosumab treatment in a follow-up of 20 of the patients from their 2010 study.[10] Therein, they described the presence of mesenchymal tissue defined as "irregular small woven bone" with some small regional transitions of this bone to new normal lamellar bone.[10] A few years later, Goldschlager et al.[2] studied a cohort of 5 patients who underwent denosumab treatment. All patients showed a radiographical response to denosumab with between 10% and 40% reduction of the tumor size, with 3 out of 4 biopsies showing no evidence of giant cells and the presence of osteoid, new bone, along with sclerotic fibro-osseous tissue.[2] Based on similar observations, other research groups have referred to denosumab-treated GCTBs as having abnormal woven osteoid forming randomly and inconsistently,[10,11,27] further described as "bone formation induced by stromal cells."[27]

While these past studies recognize that denosumab-induced elimination of giant cells is accompanied by increased mineralization and woven bone formation, this study focuses on the use of high-resolution imaging techniques to analyze this tissue with a more in-depth approach. Using qBSE we were able to evaluate precise regions of mineral content at micron to submicron levels. Our results uncover microarchitectural abnormalities in the bone structures formed with changes in the trabecular bone structure most apparent as an increase in BV/TV. Moreover, we identified an increase in mineralization from levels before denosumab treatment observed using clinical CT, suggesting levels may approach or exceed normal when GCTBs are treated with denosumab. Lamellar bone formation is slow,[42] reaching half its mineral content in about 10 d, then slowing down and increasing over the span of years.[43] Alternatively, woven bone may form where no previous bone matrix was present,[44] with a matrix laid down quickly (4 $\mu$m per day or more) resulting in high mineralization compared to its lamellar counterpart.[42] Our study facilitated localized regional analysis of mineral content changes with respect to bone type. The observed increased mineral content in woven bone compared to lamellar bone implies that lamellar bone formation occurs after woven. When combined, these 2 techniques provide insight into the effects of denosumab on bone formation and mineralization and are consistent with the proposed reduction in mechanical integrity due to increased heterogeneity of the tissue.[45] With the addition of FE-EPMA, we further evaluated the types of minerals forming, identifying differences in the Ca/P ratio, implying a potential amorphous or impure mineral structure in disorganized bone, with the transition to a more crystalline structure with time.

Within a lamellar matrix, osteocytes appear oriented along the longitudinal axis of the lamellae.[46] Osteocytes in woven bone, referred to as mesenchymal osteoblasts,[44] are randomly organized and oriented due to quick and disorganized differentiation of osteoblasts to osteocytes.[46,47] Not only do they appear in the bone matrix with random orientations, but they tend to be more circular in shape due to minor axis elongation of lacunae.[44] Our observations in denosumab-treated GCTBs showed rapid new bone formation, with highly mineralized woven bone, which is higher in mineral content than the adjacent new lamellar matrix present in the same samples, agreeing with past literature.[47,48] As a result of this random and sudden entrapment are round-shaped lacunae, with increased density,[44] visualized in this study through BSE images in SEM. We attributed the increase in circularity to a decrease in axis ratio (a result of a minor axis elongation), similarly discussed by Shapiro et al.[44] who described an axis length ratio of 1.8:1 in woven bone, a value lower than a ratio of 3.5:1 observed in lamellar bone.

Trabecular bone is mostly formed by collagen fiber bundles that align in the direction of forces to increase their

resistance to fracture,[45,49] very similar to compact lamellar bone structure.[50] These aligned collagen fiber bundles result in a striated light-dark pattern when observed under polarized light microscopy (PLM).[51] Alternatively, woven bone contains loosely packed, randomly oriented collagen fibers,[44,48] with matrix formation and mineralization occurring in all directions surrounding the cells.[44,52] While demonstrated using many techniques, the discontinuity of the collagen fibers in woven bone occurs due to random orientation and loose packing, resulting in the collagen fibers in the disorganized bone appearing shorter. Combined with decreased thickness in the collagen III fiber bundles, they become less prominent when viewed under PLM and SHG but are still accompanied by adjacent lamellar fibers. When viewed under SEM, we observed lamellar bone formation on the surfaces of woven bone, aligning with observations of woven to lamellar bone transitions with the lamellar bone formation on top of the woven bone matrix.[44] Moreover, SHG was optimized to target the visualization of collagen fiber alignment, where we demonstrated an irregular collagen organization consistent with woven bone. These same observations were made under bright-light microscopy using Sirius red-stained sections viewed under PLM, with these long sheet-like striations of lamellar bone forming on top of the woven bone in the GCTB samples. These abnormalities are attributed to denosumab treatment with indications of a state of bone repair within the re-mineralized tissue, suggesting the response after suppressing RANK signaling by denosumab treatment triggers traditional repair mechanisms in bone.

The molecular description of woven bone refers to a matrix composed primarily of collagen I.[45,46] Strikingly, our protein analysis, further confirmed through IHC, revealed increased collagen III content in the mineralized matrix of denosumab-treated GCTBs. This predominant presence of collagen III was also recently described in woven bone induced by prostate cancer metastasis to the spine.[30] This compositional difference compared with the traditional description of woven bone, could be a result of studies that traditionally describe bone repair and the presence of woven bone focusing on fracture of diaphysis of long bones as a model.[42,48] Long bone diaphysis is composed of thick cortical bone with the bone marrow confined to the medullary space, while vertebral tissue is primarily comprised of trabecular bone with a predominant medullar space. Collagen III is a primary component of reticular fibers, which compose the stroma of different organs allowing the organization of parenchymal cells and structures.[53] Collagen III is also especially abundant in the stroma of liver and bone marrow,[53] and is essential for the organization and distribution of hematopoietic cells. As such, it is not surprising that collagen III is an essential part of the repair process in bone marrow-rich trabecular bone, while cortical bone repair, where bone marrow is absent, depends on collagen I formation.

Due to the low incidence of GCTBs, the primary limitation of the current study is the small sample size, coupled with a nonrandomized population of patients with resectable tumors. Furthermore, the variance in both sex and age prevents generalization; however, incorporating exclusion criteria for such a study is not possible due to the rarity of obtaining postoperative GCTB tissue samples. To increase the confidence and statistical power of our conclusions, additional studies are required that increase sample size while maintaining variance in denosumab treatment time. This would help improve our understanding of the effects of treatment time on bone mineral characteristics, advising on optimal denosumab treatment time. Furthermore, a thorough investigation into paired effects of a patient's age and sex on response to denosumab with mineralization outcomes is warranted, providing a better understanding of screening mechanisms to predict a patient's response to denosumab treatment.

In conclusion, while rare, GCTBs have life-changing effects on patients both pre- and postoperatively. Denosumab treatment facilitates tumor ossification, alleviating pain and improving surgical margins. Our findings indicate that denosumab is associated with the formation of a disorganized, woven bone matrix in place of the GCTB. Additionally, the observed transition from woven to lamellar bone suggests a resumption of normal remodeling after treatment cessation. While many characteristics of woven bone align with the observed phenomena in mineralized GCTB treated with denosumab, heterotopic ossification is a type of "formation of extraskeletal bone in muscle and soft tissue"[54] regions. This bone formation mechanism also results in woven bone formation, accompanied by lamellar maturation.[54,55]The tumors included in this study were primarily bone resected from vertebral bodies mineralized during denosumab treatment; however, some cases of tumor expansion beyond the original bone structure did occur, and in those cases, we may observe bone formed as a result of heterotopic ossification instead of from denosumab treatment and inhibition of osteoclast function.

It is well known that osteoblasts and osteocytes secrete RANKL, which binds to its receptor RANK on osteoclast precursors, promoting osteoclast differentiation and activity. Denosumab functions similarly to the natural inhibitor osteoprotegerin (OPG) by binding with RANKL, blocking the RANKL-RANK pathway.[56] In addition to the known role of RANKL in promoting osteoclast differentiation, a recent study suggested a reverse pathway that also affects osteoblast differentiation.[57] In this reverse pathway, maturing osteoclasts secrete small extracellular vesicles that contain RANK.[58] These vesicles bind to osteoblastic RANKL, activating osteoblastic differentiation and osteogenesis.[58] While denosumab is known for blocking the extracellular RANKL-RANK binding process, its effects on this reverse pathway, including interactions with extracellular vesicles remain unclear. Therefore, further effects of denosumab on osteoblasts remain an open question and require further investigation. Overall, our in-depth analysis employed high-resolution techniques; however, the small cohort size limits the statistical power and confidence of our conclusions. Larger cohort studies are necessary to fully understand the effects of treatment duration and age on bone mineralization and formation.

## Acknowledgments

We thank the patients and their families, along with the donors and their families of the University of British Columbia (UBC) Body Donor Program, and the contributions of Matthew Tinney, Grant Reiger, and staff. We would also like to thank the UBC Bioimaging Facility (BIF, RRID: SCR_021304) for providing training and use of their FV1000 Olympus microscope, used to complete the SHG multiphoton imaging presented in this study, contributions of Heli Eunike of the UBC Materials Engineering Department for providing training and use of the SEM, contributions of Anette von der Handt of UBC Earth and Ocean Sciences for providing training and assistance with FE-EPMA, Hans Adomat and The Vancouver Prostate Centre Pathology Core for

TMT mass spectroscopy support and Danmei Liu of the Centre for Aging SMART for providing training and assistance of the $\mu$CT. The authors acknowledge the land on which this work was completed in the unceded territory of the Coast Salish Peoples, including the territories of the xwməθkwəy̓əm (Musqueam), Skwxwú7mesh (Squamish), Stó:lō and Sḵwx̱wú7mesh (Squamish), Stó:lō and Səl̓ílwətaʔ/Selilwitulh (Tsleil-Waututh) Nations.

## Author contributions

Robyn Birch (Conceptualization, Data curation, Formal analysis, Investigation, Methodology, Visualization, Writing—original draft, Writing—review & editing), Felipe Eltit (Conceptualization, Investigation, Methodology, Validation, Writing—original draft, Writing—review & editing), Dennis Xie (Data curation, Formal analysis), Qiong Wang (Data curation), Nicolas Dea (Conceptualization, Investigation, Writing—review & editing), Charles G. Fisher (Conceptualization, Investigation, Writing—review & editing), Michael E. Cox (Funding acquisition, Validation, Writing—review & editing), Tony Ng (Conceptualization, Investigation, Writing—review & editing), Raphaële Charest-Morin (Conceptualization, Funding acquisition, Investigation, Project administration, Supervision, Validation, Writing—original draft, Writing—review & editing), and Rizhi Wang (Conceptualization, Funding acquisition, Investigation, Project administration, Resources, Supervision, Validation, Writing—review & editing)

## Supplementary material

Supplementary material is available at *JBMR Plus* online.

## Funding

Operating funds were provided by a 2020 AOSpine Young Investigator Award, and a 2019 Canadian Orthopaedic Foundation – Robert B. Salter Award. The Canadian Institutes of Health Research (CIHR, Grant PJT-178280) also partially supported this study. R.B. received support from an NSERC CGS-M award, and the CREATE Training Program in 3D Printing Technology and Materials from the Natural Sciences and Engineering Research Council of Canada (NSERC). D.X. was partially funded by a Biotalent Grant. F.E. was supported by a Prostate Cancer Foundation Young Investigator Award.

## Conflicts of interest

R.C.M has received research support from a 2024 AOSpine Knowledge Forum Associate Research Award, AOSpine, the Canadian Orthopaedic Foundation, a 2023 NASS translational award, a 2023 New Frontiers in Research Exploration Award, a 2023 Vancouver Coastal Health Research Institute Investigator Award, and a 2022 AOSpine DIA, they serve on the advisory board for Cerapedics Education Event as a co-chair, is co-chairing a Stryker educational event, and a CarboFix-joint solutions educational event. N.D. has been a consultant for Baxter, Cerapedics, and Stryker, owns stock in Medtronic, and has fellowship support paid to their institution from AOSpine, Medtronic, and Depuy Synthes. C.F. has been a consultant for Medtronic, is awarded royalties from Medtronic, and has fellowship support paid to their institution from AOSpine, Medtronic, and Depuy Synthes.

## Data availability

The data underlying this article will be shared on reasonable request to the corresponding author.

## References

1. Xara-Leite F, Coutinho L, Fleming C, et al. Can denosumab cure giant cell tumors of the spine? A case report and literature review. *Eur J Orthop Surg Traumatol*. 2020;30(1):19–23. https://doi.org/10.1007/s00590-019-02554-9
2. Goldschlager T, Dea N, Boyd M, et al. Giant cell tumors of the spine: has denosumab changed the treatment paradigm? *J Neurosurg Spine*. 2015;22(5):526–533. https://doi.org/10.3171/2014.10.SPINE13937
3. Liede A, Bach BA, Stryker S, et al. Regional variation and challenges in estimating the incidence of giant cell tumor of bone. *J Bone Joint Surg Am*. 2014;96(23):1999–2007. https://doi.org/10.2106/JBJS.N.00367
4. Amelio JM, Rockberg J, Hernandez RK, et al. Population-based study of giant cell tumor of bone in Sweden (1983–2011). *Cancer Epidemiol*. 2016;42:82–89. https://doi.org/10.1016/j.canep.2016.03.014
5. Dahlin DC, Cupps RE, Johnson EW. Giant-cell tumor: a study of 195 cases. *Cancer*. 1970;25(5):1061–1070. https://doi.org/10.1002/1097-0142(197005)25:5<1061::AID-CNCR2820250509>3.0.CO;2-E
6. Minato K, Hirano T, Kawashima H, et al. Minimally invasive spinal stabilization with denosumab before total spondylectomy for a collapsing lower lumbar spinal giant cell tumor. *Acta Med Okayama*. 2021;75(1):95–101. https://doi.org/10.18926/AMO/61442
7. Goldenberg RR, Campbell CJ, Bonfiglio M. Giant-cell tumor of bone: an analysis of two hundred and eighteen cases. *J Bone Joint Surg Am*. 1970;52(4):619–664. https://doi.org/10.2106/00004623-197052040-00001
8. Larsson SE, Lorentzon R, Boquist L. Giant-cell tumor of bone: a demographic, clinical, and histopathological study of all cases recorded in the Swedish cancer registry for the years 1958 through 1968. *J Bone Joint Surg Am*. 1975;57(2):167–173. https://doi.org/10.2106/00004623-197557020-00007
9. Thomas D, Henshaw R, Skubitz K, et al. Denosumab in patients with giant-cell tumor of bone: an open-label, phase 2 study. *Lancet Oncol*. 2010;11(3):275–280. https://doi.org/10.1016/S1470-2045(10)70010-3
10. Branstetter DG, Nelson SD, Manivel JC, et al. Denosumab induces tumor reduction and bone formation in patients with giant-cell tumor of bone. *Clin Cancer Res*. 2012;18(16):4415–4424. https://doi.org/10.1158/1078-0432.CCR-12-0578
11. Boriani S, Cecchinato R, Cuzzocrea F, Bandiera S, Gamarotti M, Gasbarrini A. Denosumab in the treatment of giant cell tumor of the spine: preliminary report, review of the literature, and protocol proposal. *Eur Spine J*. 2019;29(2):257–271. https://doi.org/10.1007/s00586-019-05997-0
12. Charest-Morin R, Fisher C, Sahgal A, et al. Primary bone tumor of the spine—an evolving field: what a general spine surgeon should know. *Global Spine J*. 2019;9(1_suppl):108S–116S. https://doi.org/10.1177/2192568219828727
13. Behjati S, Tarpey PS, Presneau N, et al. Distinct *H3F3A* and *H3F3B* driver mutations define chondroblastoma and giant cell tumor of bone. *Nat Genet*. 2013;45(12):1479–1482. https://doi.org/10.1038/ng.2814
14. Cowan R, Singh G. Giant cell tumor of bone: a basic science perspective. *Bone*. 2013;52(1):238–246. https://doi.org/10.1016/j.bone.2012.10.002
15. Roux S, Amazit L, Meduri G, Guiochon-Mantel A, Milgrom E, Mariette X. RANK (receptor activator of nuclear factor kappa B) and RANK ligand are expressed in giant cell tumors of bone. *Am J Clin Pathol*. 2002;117(2):210–216. https://doi.org/10.1309/BPET-F2PE-P2BD-J3P3
16. Dempster D, Lambing C, Kostenuik P, Grauer A. Role of RANK ligand and denosumab, a targeted RANK ligand inhibitor, in bone health and osteoporosis: a review of preclinical and clinical data. *Clin Ther*. 2012;34(3):521–536. https://doi.org/10.1016/j.clinthera.2012.02.002
17. Doggrell R. Good clinical endpoints with denosumab in osteoporosis and cancer. *Expert Opin Pharmacother*. 2009;10(17):2939–2943. https://doi.org/10.1517/14656560903365197

18. Haque A, Moatasim A. Giant cell tumor of bone: a neoplasm or a reactive condition? *Int J Clin Exp Pathol*. 2008;1(6):489–501.
19. Charest-Morin R, Fisher CG, Varga PP, et al. En bloc resection versus intralesional surgery in the treatment of giant cell tumor of the spine. *Spine*. 2017;42(18):1383–1390. https://doi.org/10.1097/BRS.0000000000002094
20. Chawla S, Henshaw R, Seeger L, et al. Safety and efficacy of denosumab for adults and skeletally mature adolescents with giant cell tumor of bone: interim analysis of an open-label, parallel-group, phase 2 study. *Lancet Oncol*. 2013;14(9):901–908. https://doi.org/10.1016/S1470-2045(13)70277-8
21. Amgen. *XGEVA (Denosumab)*. 2018.
22. Turcotte R. Giant cell tumor of bone. *Orthop Clin North Am*. 2006;37(1):35–51. https://doi.org/10.1016/j.ocl.2005.08.005
23. Dubory A, Missenard G, Domont J, Court C. Interest of denosumab for the treatment of giant-cell tumors and aneurysmal bone cysts of the spine: about nine cases. *Spine*. 2016;41(11):E654–E660. https://doi.org/10.1097/BRS.0000000000001350
24. Matchuk GR, Patel DB, White EA, Menendez LR. Giant cell tumor: rapid recurrence after cessation of long-term denosumab therapy. *Skeletal Radiol*. 2015;44(7):1027–1031. https://doi.org/10.1007/s00256-015-2117-5
25. Anastasilakis A, Makras P, Yavropoulou M, Tabacco G, Naciu A, Palermo A. Denosumab discontinuation and the rebound phenomenon: a narrative review. *J Clin Med*. 2021;10(1):1–28. https://doi.org/10.3390/jcm10010152
26. Palmerini E, Picci P, Reichardt P, Downey G. Malignancy in giant cell tumor of bone: a review of the literature. *Technol Cancer Res Treat*. 2019;18:1–9. https://doi.org/10.1177/1533033819840000
27. Li H, Gao J, Gao Y, Lin N, Zheng M, Ye Z. Denosumab in giant cell tumor of bone: current status and pitfalls. *Front Oncol*. 2020;10:1–10. https://doi.org/10.3389/fonc.2020.580605
28. Kato I, Furuya M, Matsuo K, Kawabata Y, Tanaka R, Ohashi K. Giant cell tumors of bone treated with denosumab: histological, immunohistochemical and *H3F3A* mutation analyses. *Histopathology*. 2018;72(6):914–922. https://doi.org/10.1111/his.13448
29. Schindelin J, Arganda-Carreras I, Frise E, et al. FIJI: an open-source platform for biological-image analysis. *Nat Methods*. 2012;9(7):676–682. https://doi.org/10.1038/nmeth.2019
30. Eltit F, Wang Q, Jung N, et al. Sclerotic prostate cancer bone metastasis: woven bone lesions with a twist. *JBMR Plus*. 2024;8(10):1–13. https://doi.org/10.1093/jbmrpl/ziae091
31. Ayres C, Bowlin G, Henderson S, et al. Modulation of anisotropy in electrospun tissue-engineering scaffolds: analysis of fiber alignment by the fast Fourier transform. *Biomaterials*. 2006;27(32):5524–5534. https://doi.org/10.1016/j.biomaterials.2006.06.014
32. Alexander J, Fuss B, Colello R. Electric field-induced astrocyte alignment directs neurite outgrowth. *Neuron Glia Biol*. 2006;2(2):93–103. https://doi.org/10.1017/S1740925X0600010X
33. Hoshi K, Ejiri S, Ozawa H. Localizational alterations of calcium, phosphorus, and calcification-related organics such as proteoglycans and alkaline phosphatase during bone calcification. *JBMR*. 2001;16(2):289–298. https://doi.org/10.1359/jbmr.2001.16.2.289
34. Tashima T, Nagatoishi S, Sagara H, Ohnuma S, Tsumoto K. Osteomodulin regulates diameter and alters shape of collagen fibrils. *Biochem Biophys Res Commun*. 2015;463(3):292–296. https://doi.org/10.1016/j.bbrc.2015.05.053
35. Deshpande AS, Fang PA, Zhang X, Jayaraman T, Sfeir C, Beniash E. Primary structure and phosphorylation of dentin matrix protein 1 (DMP1) and dentin phosphophoryn (DPP) uniquely determine their role in biomineralization. *Biomacromolecules*. 2011;12(8):2933–2945. https://doi.org/10.1021/bm2005214
36. Hunter G. Role of osteopontin in modulation of hydroxyapatite formation. *Calcif Tissue Int*. 2013;93(4):348–354. https://doi.org/10.1007/s00223-013-9698-6
37. Sodek J, Ganss B, McKee MD. Osteopontin. *Crit Rev Oral Biol Med*. 2000;11(3):279–303. https://doi.org/10.1177/10454411000110030101
38. McClung MR, Lewiecki EM, Cohen SB, et al. Denosumab in postmenopausal women with low bone mineral density. *N Engl J Med*. 2006;354(8):821–831. https://doi.org/10.1056/NEJMoa044459
39. Miller PD, Bolognese MA, Lewiecki ML, et al. Effect of denosumab on bone density and turnover in postmenopausal women with low bone mass after long-term continued, discontinued, and restarting of therapy: a randomized blinded phase 2 clinical trial. *Bone*. 2008;43(2):222–229. https://doi.org/10.1016/j.bone.2008.04.007
40. Bone HG, Bolognese MA, Yuen CK, et al. Effects of denosumab treatment and discontinuation on bone mineral density and bone turnover markers in postmenopausal women with low bone mass. *J Clin Endocrinol Metab*. 2011;96(4):972–980. https://doi.org/10.1210/jc.2010-1502
41. Cummings SR, Martin JS, McClung MR, et al. Denosumab for prevention of fractures in postmenopausal women with osteoporosis. *N Engl J Med*. 2009;361(8):756–765. https://doi.org/10.1056/NEJMoa0809493
42. Curry J. Chapter One: The structure of bone tissue. In: *Bones: Structure and Mechanics*. Princeton, NJ: Princeton University Press; 2006.
43. Fratzl P, Gupta H, Paschalis E, Roschger P. Structure and mechanical quality of the collagen-mineral nano-composite in bone. *J Mater Chem*. 2004;14(14):2115–2123. https://doi.org/10.1039/B402005G
44. Shapiro F, Wu J. Woven bone overview: structural classification based on its integral role in developmental, repair, and pathological bone formation throughout vertebrate groups. *Eur Cells Mater*. 2019;38:137–167. https://doi.org/10.22203/eCM.v038a11
45. Burr DB. Bone morphology and organization. In: *Basic Bone Biology and Physiology*. Academic Press.
46. Marotti G, Ferretti M, Palumba C. The problem of bone lamellation: an attempt to explain different proposed models. *J Morphol*. 2013;274(5):543–550. https://doi.org/10.1002/jmor.20114
47. Marotti G. A new theory of bone lamellation. *Calcif Tissue Int*. 1993;53(S1):S47–S56. https://doi.org/10.1007/BF01673402
48. Weiner S, Wagner H. The material bone: structure-mechanical function relations. *Annu Rev Mater Res*. 1998;28(1):271–298. https://doi.org/10.1146/annurev.matsci.28.1.271
49. Wolff J. *The Law of Bone Remodelling*. 1st ed. Springer-Verlag; 1986.
50. Reznikov N, Chase H, Brumfeld V, Shahar R, Weiner S. The 3D structure of the collagen fibril network in human trabecular bone: relation to trabecular organization. *Bone*. 2015;71:189–195. https://doi.org/10.1016/j.bone.2014.10.017
51. Rho JY, Kuhn-Spearing L, Zioupos P. Mechanical properties and the hierarchical structure of bone. *Med Eng Phys*. 1998;20(2):92–102. https://doi.org/10.1016/S1350-4533(98)00007-1
52. Gorski J. Is all bone the same? Distinctive distributions and properties of non-collagenous matrix proteins in lamellar vs. woven bone imply the existence of different underlying osteogenic mechanisms. *Crit Rev Oral Biol Med*. 1998;9(2):201–223. https://doi.org/10.1177/10454411980090020401
53. Gartner L. *Textbook of Histology*. 5th ed. Elsevier, Inc.; 2021.
54. Meyers C, Lisiecki J, Miller S, et al. Heterotopic ossification: a comprehensive review. *JBMR Plus*. 2019;3(4):e10172. https://doi.org/10.1002/jbm4.10172
55. Schena F, Menale C, Caci E, et al. Murine Rankl−/− mesenchymal stromal cells display an osteogenic differentiation defect improved by a RANKL-expressing lentiviral vector. *Stem Cells*. 2017;35(5):1365–1377. https://doi.org/10.1002/stem.2574
56. Ikebuchi Y, Aoki S, Honma M, et al. Coupling of bone resorption and formation by RANKL reverse signalling. *Nature*.

2018;561(7722):195–200. https://doi.org/10.1038/s41586-018-0482-7

57. Cocks M, Mohan A, Meyers CA, et al. Vascular patterning in human heterotopic ossification. *Hum Pathol*. 2017;63:165–170. https://doi.org/10.1016/j.humpath.2017.03.005

58. Schieferdecker A, Voigt M, Riecken K, et al. Denosumab mimics the natural decoy receptor osteoprotegerin by interacting with its major binding site on RANKL. *Oncotarget*. 2014;5(16):6647–6653. https://doi.org/10.18632/oncotarget.2160